Improved measurement of vibration amplitude in dynamic optical coherence elastography

Brendan F. Kennedy,[1,*] Maciej Wojtkowski,[2] Maciej Szkulmowski,[2]
Kelsey M. Kennedy,[1] Karol Karnowski,[2] and David D. Sampson[1,3]

[1]Optical+Biomedical Engineering Laboratory, School of Electrical, Electronic and Computer Engineering,
The University of Western Australia, 35 Stirling Highway, Crawley, Western Australia 6009, Australia
[2]Institute of Physics, Nicolaus Copernicus University, ul. Grudziadzka 5, PL87-100 Torun, Poland
[3]Centre for Microscopy, Characterisation and Analysis, The University of Western Australia, 35 Stirling Highway,
Crawley, Western Australia, 6009, Australia
**brendan.kennedy@uwa.edu.au*

Abstract: Optical coherence elastography employs optical coherence tomography (OCT) to measure the displacement of tissues under load and, thus, maps the resulting strain into an image, known as an elastogram. We present a new improved method to measure vibration amplitude in dynamic optical coherence elastography. The tissue vibration amplitude caused by sinusoidal loading is measured from the spread of the Doppler spectrum, which is extracted using joint spectral and time domain signal processing. At low OCT signal-to-noise ratio (SNR), the method provides more accurate vibration amplitude measurements than the currently used phase-sensitive method. For measurements performed on a mirror at OCT SNR = 5 dB, our method introduces <3% error, compared to >20% using the phase-sensitive method. We present elastograms of a tissue-mimicking phantom and excised porcine tissue that demonstrate improvements, including a 50% increase in the depth range of reliable vibration amplitude measurement.

OCIS codes: (110.4500) Optical coherence tomography; (290.5820) Scattering measurements; (170.6935) Tissue characterization.

References and links

1. J. M. Schmitt, "OCT elastography: imaging microscopic deformation and strain of tissue," Opt. Express **3**(6), 199–211 (1998).
2. J. Ophir, I. Céspedes, H. Ponnekanti, Y. Yazdi, and X. Li, "Elastography: a quantitative method for imaging the elasticity of biological tissues," Ultrason. Imaging **13**(2), 111–134 (1991).
3. R. Muthupillai, D. J. Lomas, P. J. Rossman, J. F. Greenleaf, A. Manduca, and R. L. Ehman, "Magnetic resonance elastography by direct visualization of propagating acoustic strain waves," Science **269**(5232), 1854–1857 (1995).
4. W. Drexler and J. G. Fujimoto, *Optical Coherence Tomography: Technology and Applications* (Springer-Verlag, Berlin, 2008).
5. B. F. Kennedy, S. H. Koh, R. A. McLaughlin, K. M. Kennedy, P. R. T. Munro, and D. D. Sampson, "Strain estimation in phase-sensitive optical coherence elastography," Biomed. Opt. Express **3**(8), 1865–1879 (2012).
6. R. C. Chan, A. H. Chau, W. C. Karl, S. Nadkarni, A. S. Khalil, N. Iftimia, M. Shishkov, G. J. Tearney, M. R. Kaazempur-Mofrad, and B. E. Bouma, "OCT-based arterial elastography: robust estimation exploiting tissue biomechanics," Opt. Express **12**(19), 4558–4572 (2004).
7. J. Rogowska, N. A. Patel, J. G. Fujimoto, and M. E. Brezinski, "Optical coherence tomographic elastography technique for measuring deformation and strain of atherosclerotic tissues," Heart **90**(5), 556–562 (2004).
8. B. F. Kennedy, T. R. Hillman, A. Curatolo, and D. D. Sampson, "Speckle reduction in optical coherence tomography by strain compounding," Opt. Lett. **35**(14), 2445–2447 (2010).
9. B. F. Kennedy, A. Curatolo, T. R. Hillman, C. M. Saunders, and D. D. Sampson, "Speckle reduction in optical coherence tomography images using tissue viscoelasticity," J. Biomed. Opt. **16**(2), 020506 (2011).
10. T. R. Hillman, A. Curatolo, B. F. Kennedy, and D. D. Sampson, "Detection of multiple scattering in optical coherence tomography by speckle correlation of angle-dependent B-scans," Opt. Lett. **35**(12), 1998–2000 (2010).
11. R. K. Wang, Z. H. Ma, and S. J. Kirkpatrick, "Tissue Doppler optical coherence elastography for real time strain rate and strain mapping of soft tissue," Appl. Phys. Lett. **89**(14), 144103 (2006).

12. B. Park, M. C. Pierce, B. Cense, S. H. Yun, M. Mujat, G. J. Tearney, B. E. Bouma, and J. F. de Boer, "Real-time fiber-based multi-functional spectral-domain optical coherence tomography at 1.3 μm," Opt. Express **13**(11), 3931–3944 (2005).
13. A. Szkulmowska, M. Szkulmowski, A. Kowalczyk, and M. Wojtkowski, "Phase-resolved Doppler optical coherence tomography—limitations and improvements," Opt. Lett. **33**(13), 1425–1427 (2008).
14. K. M. Kennedy, B. F. Kennedy, R. A. McLaughlin, and D. D. Sampson, "Needle optical coherence elastography for tissue boundary detection," Opt. Lett. **37**(12), 2310–2312 (2012).
15. X. Liang, A. L. Oldenburg, V. Crecea, E. J. Chaney, and S. A. Boppart, "Optical micro-scale mapping of dynamic biomechanical tissue properties," Opt. Express **16**(15), 11052–11065 (2008).
16. S. G. Adie, X. Liang, B. F. Kennedy, R. John, D. D. Sampson, and S. A. Boppart, "Spectroscopic optical coherence elastography," Opt. Express **18**(25), 25519–25534 (2010).
17. X. Liang, S. G. Adie, R. John, and S. A. Boppart, "Dynamic spectral-domain optical coherence elastography for tissue characterization," Opt. Express **18**(13), 14183–14190 (2010).
18. B. F. Kennedy, X. Liang, S. G. Adie, D. K. Gerstmann, B. C. Quirk, S. A. Boppart, and D. D. Sampson, "*In vivo* three-dimensional optical coherence elastography," Opt. Express **19**(7), 6623–6634 (2011).
19. A. L. Oldenburg, V. Crecea, S. A. Rinne, and S. A. Boppart, "Phase-resolved magnetomotive OCT for imaging nanomolar concentrations of magnetic nanoparticles in tissues," Opt. Express **16**(15), 11525–11539 (2008).
20. D. C. Adler, S. W. Huang, R. Huber, and J. G. Fujimoto, "Photothermal detection of gold nanoparticles using phase-sensitive optical coherence tomography," Opt. Express **16**(7), 4376–4393 (2008).
21. R. K. Wang and A. L. Nuttall, "Phase-sensitive optical coherence tomography imaging of the tissue motion within the organ of Corti at a subnanometer scale: a preliminary study," J. Biomed. Opt. **15**(5), 056005 (2010).
22. B. F. Kennedy, T. R. Hillman, R. A. McLaughlin, B. C. Quirk, and D. D. Sampson, "*In vivo* dynamic optical coherence elastography using a ring actuator," Opt. Express **17**(24), 21762–21772 (2009).
23. C. Li, Z. Huang, and R. K. Wang, "Elastic properties of soft tissue-mimicking phantoms assessed by combined use of laser ultrasonics and low coherence interferometry," Opt. Express **19**(11), 10153–10163 (2011).
24. C. Li, G. Guan, X. Cheng, Z. Huang, and R. K. Wang, "Quantitative elastography provided by surface acoustic waves measured by phase-sensitive optical coherence tomography," Opt. Lett. **37**(4), 722–724 (2012).
25. R. K. Manapuram, S. R. Aglyamov, F. M. Monediado, M. Mashiatulla, J. Li, S. Y. Emelianov, and K. V. Larin, "*In vivo* estimation of elastic wave parameters using phase-stabilized swept source optical coherence elastography," J. Biomed. Opt. **17**(10), 100501 (2012).
26. X. Liang, M. Orescanin, K. S. Toohey, M. F. Insana, and S. A. Boppart, "Acoustomotive optical coherence elastography for measuring material mechanical properties," Opt. Lett. **34**(19), 2894–2896 (2009).
27. M. Razani, A. Mariampillai, C. Sun, T. W. H. Luk, V. X. D. Yang, and M. C. Kolios, "Feasibility of optical coherence elastography measurements of shear wave propagation in homogeneous tissue equivalent phantoms," Biomed. Opt. Express **3**(5), 972–980 (2012).
28. D. C. Ghiglia and M. D. Pritt, *Two-Dimensional Phase Unwrapping: Theory, Algorithms, and Software* (Wiley, New York, 1998).
29. M. Szkulmowski, A. Szkulmowska, T. Bajraszewski, A. Kowalczyk, and M. Wojtkowski, "Flow velocity estimation using joint Spectral and Time domain Optical Coherence Tomography," Opt. Express **16**(9), 6008–6025 (2008).
30. M. Szkulmowski, I. Grulkowski, D. Szlag, A. Szkulmowska, A. Kowalczyk, and M. Wojtkowski, "Flow velocity estimation by complex ambiguity free joint Spectral and Time domain Optical Coherence Tomography," Opt. Express **17**(16), 14281–14297 (2009).
31. S. G. Adie, B. F. Kennedy, J. J. Armstrong, S. A. Alexandrov, and D. D. Sampson, "Audio frequency *in vivo* optical coherence elastography," Phys. Med. Biol. **54**(10), 3129–3139 (2009).
32. D. D. Sampson and T. R. Hillman, "Optical coherence tomography," in *Lasers And Current Optical Techniques In Biology*, G. Palumbo and R. Pratesi, eds. (ESP Comprehensive Series in Photosciences, Cambridge, UK, 2004), pp. 481–571.
33. O. Sasaki and H. Okazaki, "Sinusoidal phase modulating interferometry for surface profile measurement," Appl. Opt. **25**(18), 3137–3140 (1986).
34. S. R. Huang, R. M. Lerner, and K. J. Parker, "On estimating the amplitude of harmonic vibration from the Doppler spectrum of reflected signals," J. Acoust. Soc. Am. **88**(6), 2702–2712 (1990).
35. A. Bruce Carlson, P. B. Crilly, and J. C. Rutledge, *Communications Systems* (McGraw-Hill, New York, 2002).
36. S. Haykin, *Communication Systems* (Wiley, New York, 2001).
37. K. Kristoffersen, "Time-domain estimation of the center frequency and spread of Doppler spectra in diagnostic ultrasound," IEEE Trans. Ultrason. Ferroelectr. Freq. Control **35**(6), 685–700 (1988).
38. G. Lamouche, B. F. Kennedy, K. M. Kennedy, C. E. Bisaillon, A. Curatolo, G. Campbell, V. Pazos, and D. D. Sampson, "Review of tissue simulating phantoms with controllable optical, mechanical and structural properties for use in optical coherence tomography," Biomed. Opt. Express **3**(6), 1381–1398 (2012).
39. R. N. Bracewell, *The Fourier Transform and Its Applications* (McGraw-Hill, New York, 1999).
40. M. Wojtkowski, A. Kowalczyk, R. Leitgeb, and A. F. Fercher, "Full range complex spectral optical coherence tomography technique in eye imaging," Opt. Lett. **27**(16), 1415–1417 (2002).
41. E. W. Chang, J. B. Kobler, and S. H. Yun, "Triggered optical coherence tomography for capturing rapid periodic motion," Sci. Rep. **1**, 48 (2011).

42. G. Liu, M. Rubinstein, A. Saidi, W. Qi, A. Foulad, B. Wong, and Z. Chen, "Imaging vibrating vocal folds with a high speed 1050 nm swept source OCT and ODT," Opt. Express **19**(12), 11880–11889 (2011).
43. F. Chen, D. Zha, A. Fridberger, J. Zheng, N. Choudhury, S. L. Jacques, R. K. Wang, X. Shi, and A. L. Nuttall, "A differentially amplified motion in the ear for near-threshold sound detection," Nat. Neurosci. **14**(6), 770–774 (2011).
44. E. W. Chang, J. B. Kobler, and S. H. Yun, "Subnanometer optical coherence tomographic vibrography," Opt. Lett. **37**(17), 3678–3680 (2012).

1. Introduction

Optical coherence elastography (OCE) is a technique for imaging the microscopic mechanical properties of tissue [1], with the potential to provide at least an order of magnitude improvement in spatial resolution over elastography based on ultrasound [2] or MRI [3]. In OCE, a sample is subjected to mechanical loading (stress) and the resulting local displacement is measured using optical coherence tomography (OCT) [4]. The strain, given by the slope of the displacement versus depth, is displayed in a two- or three-dimensional elastogram. Errors in the displacement measurement are amplified in the strain calculation [5], degrading the elastogram. New methods to measure displacement with improved accuracy and dynamic range will improve elastogram quality and increase OCE's potential for clinical utility.

OCE may employ either quasi-static (<10 Hz) or dynamic (>10 Hz) loading. Initially, quasi-static loading was employed and the displacement between consecutive B-scans was measured using cross correlation-based speckle-tracking algorithms [1,6,7]. However, the dynamic range of such methods is limited by speckle decorrelation [8–10]. Quasi-static, phase-sensitive OCE was proposed, in part, to overcome this limitation by improving the lower limit on displacement [11]. This method is based on the linear relationship between the phase of the OCT signal and sample motion [12,13]. Recently, a needle-based extension to quasi-static, phase-sensitive OCE has been reported [14].

In dynamic OCE, quasi-static loading and displacement measurement are replaced by sinusoidal loading and time-dependent displacement (vibration amplitude) measurement. Dynamic OCE has also employed a phase-sensitive method [15–18], which is similar to methods used in magneto-motive [19] and photothermal OCT [20], and to measure vibration in the ear [21]. For *in vivo* imaging, dynamic methods provide the opportunity to reduce motion artifacts by vibrating the tissue at frequencies above those caused by subject motion [18,22]. Dynamic phase-sensitive OCE also offers several alternative modes of measurement. Variants include: spectroscopic OCE that generates contrast through probing changes in tissue mechanical resonances [16]; measurement of shear wave velocity to extract elasticity [23–25]; and internal loading using acoustic radiation force [26,27].

Despite the prevalence of the phase-sensitive method in the dynamic OCE techniques reported to date, it has two limitations. Firstly, because the minimum detectable phase difference, *i.e.*, the phase sensitivity, is inversely proportional to the signal-to-noise ratio (SNR) of the OCT signal [12], the displacement precision reduces with depth in a scattering sample. This dependence limits the range of precise measured strain to significantly less than the OCT depth range. Secondly, the decreasing phase sensitivity with depth causes the incidence of phase wrapping to markedly increase [28]. Phase wrapping causes the mean measured displacement to tend towards zero, which leads to an underestimation of the true value [29]. This systematic error severely limits elastogram accuracy and quality.

In this paper, we propose a new method for improved vibration amplitude measurement in dynamic OCE, which is based on an analysis of the frequency tones of the Doppler spectrum obtained from a sample subjected to sinusoidal loading. Since it is related to joint spectral and time domain (STd) OCT, previously proposed for flow imaging [29,30], we refer to it as joint spectral and time domain optical coherence elastography (STdOCE). STdOCE provides more accurate vibration amplitude measurement in the case of low OCT SNR (<20 dB), which extends the depth range and significantly improves the elastogram quality. Elastograms of excised porcine tissue demonstrate a 50% increase in the depth to which strain is accurately measured.

The paper is organized as follows. In Section 2, we describe the theory of vibration amplitude and strain measurement for STdOCE and phase-sensitive OCE. In Section 3, we present the experimental setup and method. In Section 4, we demonstrate the advantage of STdOCE using results from a vibrating mirror, a tissue-mimicking phantom containing a stiff inclusion, and a section of freshly excised porcine tissue. In Sections 5 and 6, respectively, we present a discussion of the results and the main conclusions.

2. Theory

In STdOCE, two Fourier transforms are performed on data acquired with a spectral-domain (SD) OCT system. The first Fourier transform is performed in the wavenumber domain to retrieve the depth-resolved OCT signal. The second is performed in the time domain and, for a sample voxel containing vibrating components, results in a Doppler spectrum containing frequency tones. In STdOCE, these frequency tones, described by Bessel functions of the first kind, are used to extract the vibration amplitude at each depth in the sample.

STdOCE is related to a previously reported dynamic OCE method based on time-domain (TD) OCT [22,31]. That method uses the ratio of odd and/or even frequency tones to extract vibration amplitude. The bandwidth of these tones in TD-OCT increases with both the bandwidth of the optical source and the A-scan velocity [31,32], which causes them to overlap in frequency and restricts measurements to only the first few tones. This restriction limits the accuracy of the method, and requires the use of a prohibitively slow A-scan acquisition rate (~1 Hz). Furthermore, difficulties arise when a ratio of frequency tones approaches an asymptote caused by a vanishing frequency tone, unless complex post-processing techniques are employed [33]. STdOCE overcomes these limitations. The increased number of tones in the Doppler spectrum provided by SD-OCT enables use of a method closely related to one proposed in ultrasound elastography [34], in which the vibration amplitude is determined from the variance or spectral spread of frequency tones in the Doppler spectrum.

2.1. OCT signal of a vibrating sample

Consider a spectral-domain OCT system consisting of a stationary mirror in the reference arm and a mirror in the sample arm oscillating sinusoidally in the axial direction. After performing a Fourier transform on the detected OCT signal in *k*-space [4], its amplitude may be expressed as [31]

$$s(z,t) = A_z \cos\left[\varphi_{tot}(z,t)\right] = A_z \cos\left[\varphi_{DC} + \varphi_s(z,t)\sin\left(2\pi f_s t\right)\right], \tag{1}$$

where A_z is proportional to the amplitude in the sample and reference arms and the argument of the cosine function, φ_{tot}, represents the total phase of the signal. φ_{DC} is the quasi-static phase of the interferometer and f_s is the vibration frequency of the mirror. The vibration amplitude, d_s, can be determined from the maximum phase deviation, φ_s, according to [31]

$$\varphi_s(z,t) = \frac{4\pi d_s(z,t)\cos\theta}{\lambda_0}, \tag{2}$$

where θ is the angle between the incident beam and the vibrating mirror and λ_0 is the mean wavelength of the light source. The displacement of the mirror may be described by

$$d(z,t) = d_s(z,t)\sin\left(2\pi f_s t\right), \tag{3}$$

and the corresponding velocity may be expressed as

#175397 - $15.00 USD Received 31 Aug 2012; revised 5 Nov 2012; accepted 5 Nov 2012; published 7 Nov 2012

$$v(z,t) = 2\pi f_s d_s(z,t)\cos\left(2\pi f_s t\right). \tag{4}$$

The Doppler shift introduced to the detected OCT signal is given by [4]

$$f_D(z,t) = \frac{2v(z,t)\cos\theta}{\lambda_0}. \tag{5}$$

Substituting Eq. (4) into Eq. (5) allows the Doppler shift to be written in terms of the vibration amplitude, d_s, as

$$f_D(z,t) = f_m \cos\left(2\pi f_s t\right) = \frac{4\pi f_s d_s(z,t)\cos\theta}{\lambda_0}\cos\left(2\pi f_s t\right), \tag{6}$$

where f_m is the maximum Doppler shift, which is related to the phase defined in Eq. (1) by [35,36]

$$f_D(z,t) = \frac{1}{2\pi}\frac{d\varphi_{tot}}{dt}. \tag{7}$$

Equations (6) and (7) can be used to rewrite the argument of the cosine function in Eq. (1) in terms of the maximum Doppler shift:

$$s(z,t) = A_z \cos\left[\varphi_{DC} + \beta\sin\left(2\pi f_s t\right)\right], \tag{8}$$

where β is the modulation index, defined as f_m / f_s [35,36]. From Eq. (8), we observe that the amplitude of the OCT signal is modulated by the Doppler shift introduced by the vibrating mirror. The vibration amplitude of the mirror can be determined from a measurement of β. To demodulate the signal, *i.e.*, extract β from $s(z,t)$, we employ an algorithm closely related to one previously presented in the related field of sonoelasticity imaging [34].

2.2. Measuring vibration amplitude from the Doppler spectrum

Using trigonometric identities, it is possible to express Eq. (8) as a series of Bessel functions of the first kind [34,35]:

$$s(z,t) = A_z \sum_{n=-\infty}^{\infty} J_n\left(\beta\right)\cos\left(n2\pi f_s t\right), \tag{9}$$

where J_n represents the nth-order Bessel function. Importantly, Eq. (9) shows, in the case of a sinusoidally vibrating mirror, that the amplitude is not only modulated at the fundamental vibration frequency, f_s, but also at the overtones, nf_s, each weighted by the corresponding Bessel function, J_n. Fourier transforming Eq. (9) allows us to determine the Doppler power spectrum, given by

$$S\left(z,f\right) = \frac{A_z^2}{4}\sum_{n=-\infty}^{\infty} J_n^2\left(\beta\right)\left[\delta(f - nf_s) + \delta(f + nf_s)\right]. \tag{10}$$

As described previously [34], the vibration amplitude is estimated from the positive half-spectrum. The theoretical temporal waveform and positive spectral components of the vibrating signal in a single voxel are plotted in Fig. 1 based on a vibration frequency of 50 Hz and three values of β: 1.5, 3 and 6 (shown increasing from top to bottom in the figure).

For the spectrum described by Eq. (10), the mean frequency is zero, since $J_{-n}(\beta) = (-1)^n J_n(\beta)$, and the power spectrum is, thus, symmetric about zero frequency. The

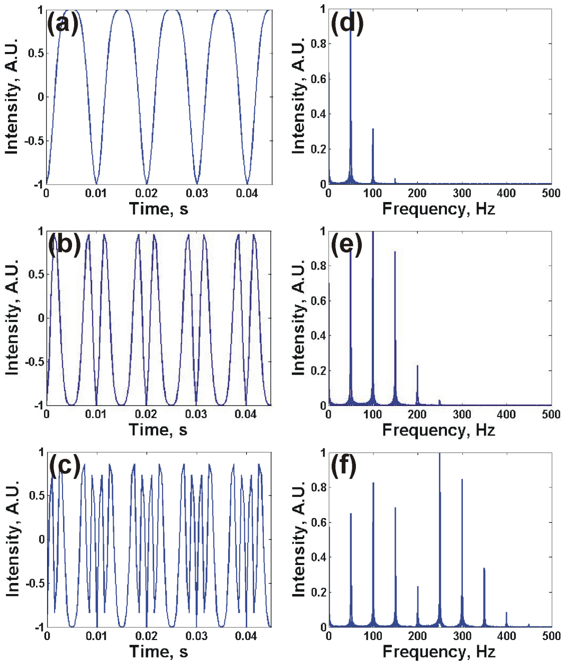

Fig. 1. Theoretical ((a)-(c)) temporal and ((d)-(f)) spectral components of an OCT signal from a mirror vibrating at 50 Hz with β equal to (a), (d) 1.5; (b), (e) 3; and (c), (f) 6.

spectral spread (or variance), σ_f^2, may be calculated from the zeroth and second moments of the spectrum, m_0 and m_2, respectively, according to [34,37]

$$\sigma_f^2 = \frac{m_2}{m_0}. \tag{11}$$

For sinusoidal modulation, it has been shown previously [34] that

$$m_0 = \sum_{n=-\infty}^{n=\infty} J_n^2(\beta) = 1, \tag{12}$$

and

$$m_2 = \sum_{n=-\infty}^{n=\infty} (nf_s)^2 J_n^2(\beta) = \frac{(\beta f)^2}{2}. \tag{13}$$

Substituting Eqs. (12) and (13) into Eq. (11) allows us to express the modulation index, β, in terms of the spectral spread [34]:

$$\beta = \frac{\sqrt{2}\sigma_f}{f_s}. \tag{14}$$

Having determined β from the Doppler spectrum, the vibration amplitude of the sample can be calculated using the analysis presented in Section 2.1. Until now, to simplify the analysis, a vibrating mirror has been considered. However, this analysis is also applicable to turbid samples under sinusoidal loading. In this case, d_s is measured at each depth in the sample and the strain, ε, may be calculated from [22]

#175397 - $15.00 USD Received 31 Aug 2012; revised 5 Nov 2012; accepted 5 Nov 2012; published 7 Nov 2012

$$\varepsilon = \frac{\Delta d_s}{\Delta z}, \tag{15}$$

where Δd_s is the change in vibration amplitude over an axial range Δz within the sample. In this paper, we calculate the strain using a weighted least squares strain estimation method described previously [5]. We then generate 2D elastograms by scanning the beam across the sample in the *x*-direction.

2.3. Phase-sensitive vibration amplitude measurement

To allow us to compare and contrast STdOCE with phase-sensitive OCE, in this subsection we briefly describe the phase-sensitive method of measuring vibration amplitude, previously presented in [21]. Consider again the case of a sinusoidally oscillating mirror described in Subsection 2.1. From Eqs. (1) and (2), the total phase of the detected OCT signal is given by

$$\varphi_{tot} = \varphi_{DC} + \frac{4\pi d_s(z,t)\cos\theta}{\lambda_0}\sin\left(2\pi f_s t\right). \tag{16}$$

Differentiation can be performed to eliminate the phase term φ_{DC}, giving

$$\Delta\varphi(z,t) = \frac{8\pi^2 d_s(z,t) f_s \Delta t \cos\theta}{\lambda_0}\cos\left(2\pi f_s t\right), \tag{17}$$

where Δt is the A-scan acquisition time. From Eq. (17), the phase difference between successive A-scans can be used to extract the vibration amplitude, $d_s(z,t)$. It has been demonstrated that the sensitivity of this method can be improved by performing a Fourier transform on the phase difference, which gives [21]

$$p(z,f) = \mathrm{FT}[(\Delta\varphi(z,t))] = \frac{(2\pi)^3}{\lambda_0} d_s(z,f_s) f_s \Delta t \cos\theta\left[\delta(f-f_s)+\delta(f+f_s)\right], \tag{18}$$

where $p(z,f)$ is the power spectral density of the phase signal. The sample vibration amplitude at the known frequency, f_s, can be calculated from the following expression:

$$d_s(z,f_s) = \frac{\left|p(z,f_s)\right|\lambda_0}{(2\pi)^3 f_s \Delta t \cos\theta}. \tag{19}$$

If d_s is measured at each depth in the sample, Eq. (15) can be used to calculate the strain. It is important to note that Eq. (19) is valid if the phase difference is correctly unwrapped. For significant wrapping errors, caused by the presence of noise, d_s is underestimated. In the next section, we describe the experimental setup and methodology used to implement the analyses described in this section.

3. Methods

3.1. Experimental setup and procedure

Results were obtained using a spectral-domain OCE system employing a superluminescent diode source with mean wavelength of 835 nm and 55.4 nm bandwidth, illuminating the sample with 10 mW of optical power. The theoretical lateral resolution is 15 μm and the sensitivity was measured to be 105 dB for an exposure time of 50 μs. The spectrometer consisted of a diffraction grating with 1800 lines/mm, a lens with a focal length of 50 mm and a line-scan camera with 4096 pixels. The sensitivity roll-off was measured to be 4 dB/mm.

#175397 - $15.00 USD Received 31 Aug 2012; revised 5 Nov 2012; accepted 5 Nov 2012; published 7 Nov 2012

The camera exposure time was 50 μs and the A-scan acquisition time was 500 μs. Lateral scanning over a 3 mm range was performed using a galvanometer mirror, driven by a sawtooth waveform. The phase sensitivity of the system is 9 mrad, for OCT SNR = 50 dB, calculated from the standard deviation of phase measured from a stationary mirror [12]. This value exceeds the theoretical minimum of 2.2 mrad because of galvanometer jitter.

Samples were mechanically loaded using a piezoelectric ring actuator, described previously [22], that enabled imaging and compression from the same side of the sample (from the top in all presented elastograms). For each sample, a refractive index of 1.4 was assumed. Samples were preloaded by compression against a rigid upper boundary to ensure full uniform contact. This was achieved by displacing the compression plate by 250 μm beyond the point of first contact. Each sample was tilted with respect to the beam axis to minimize specular reflection from the air-sample interface. To maintain uniform compression, the ring actuator compression plate and the upper rigid boundary were tilted by the same angle in both x and y planes. In all cases, a 50 Hz sinusoidal wave was applied to the actuator, resulting in unloaded vibration amplitudes of up to 0.45 μm.

3.2. Phantom fabrication

Tissue-mimicking phantoms with dimensions (length × width × height) of 10 mm × 10 mm × 2.75 mm were fabricated using room-temperature vulcanizing silicone as the bulk medium and titanium dioxide (TiO_2) as optical scatterers [38]. Two phantom designs were fabricated. Phantom 1 was designed to be optically and mechanically homogeneous. It was fabricated from soft silicone (Elastosil® P7676, Wacker, Germany) and contained 1.5 mg/ml of TiO_2 particles. Its elastic modulus was measured using an Instron materials testing system to be 25 kPa. Phantom 2 was designed to be a soft bulk medium containing hard inclusions. It was fabricated from the same silicone used in Phantom 1. Inclusions of measured average diameter of 0.4 mm were fabricated using the method presented in [5]. The inclusions contained 2.5 mg/ml TiO_2 particles and were fabricated using a harder silicone (Elastosil® RT 601, Wacker, Germany), with measured elastic modulus of 4 MPa. They were embedded in the soft surrounding silicone as described previously [5]. The base of an inclusion was located ~0.5 mm below the phantom surface.

3.3. Data Processing

3.3.1. STdOCE

Figure 2 shows the steps in the data acquisition and processing procedure. Phantom 1 was placed under load as described in Subsection 3.1. In Fig. 2(a), 2000 spectral interferograms acquired from the same lateral position in Phantom 1 are shown. These spectra are modulated in both wavenumber and time: modulation in wavenumber is caused by scattering from the sample at each depth, whilst modulation in time is caused by loading-induced motion, visible in the inset of Fig. 2(a). In Fig. 2(b), A-scans obtained by performing a Fourier transform in wavenumber are shown. Each A-scan corresponds to the standard Fourier transform performed in SD-OCT to obtain depth-resolved measurements [4]. The sample motion at the position indicated by the green box is visible in the inset of Fig. 2(b).

In STdOCE, a second Fourier transform is performed in the time domain, *i.e.*, at each depth in the set of A-scans, in order to access the Doppler spectrum. In Fig. 3(c), the Doppler spectrum due to motion at the depth indicated by the red line in Fig. 3(b) is shown, with nine overtones in evidence. The frequency resolution of the sampled Doppler spectrum is determined by the ratio between the A-scan sampling frequency and the number of points, *i.e.*, A-scans, in the Fourier transform. Furthermore, the highest measurable frequency is set by the Nyquist sampling criterion, *i.e.*, half the A-scan sampling frequency [39]. Also, the range over which the frequency tones can be unambiguously detected is halved by the well-known

#175397 - $15.00 USD Received 31 Aug 2012; revised 5 Nov 2012; accepted 5 Nov 2012; published 7 Nov 2012

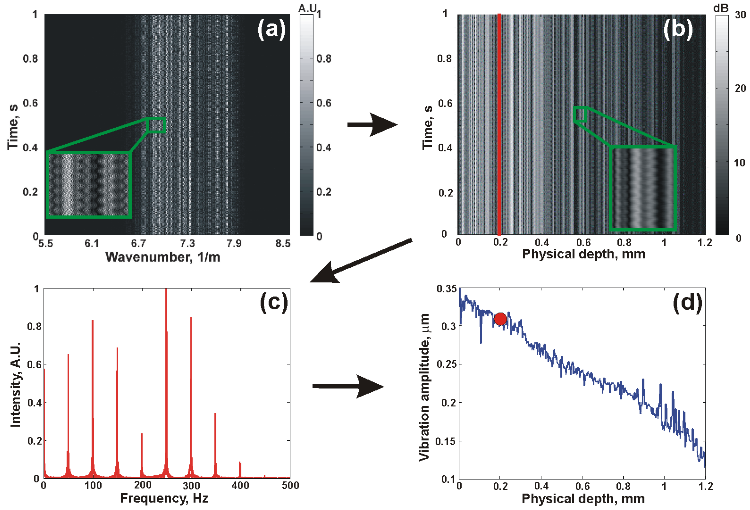

Fig. 2. Data processing procedure for STdOCE: (a) 2000 spectral interferograms resampled to *k*-space; (b) A-scans obtained after Fourier transform in *k*-space; (c) Doppler spectrum after Fourier transform in time, performed at depth indicated by the red line in (b); and (d) Vibration amplitude calculated using the spectral spread algorithm. The red dot in (d) corresponds to the vibration amplitude calculated from the Doppler spectrum in (c).

complex ambiguity problem [40]. These points need to be considered to ensure the highest overtone is adequately sampled.

Having calculated the Doppler spectrum, the spectral spread algorithm described in Subsection 2.2 is used to calculate the vibration amplitude. Specifically, σ_f is calculated from the Doppler spectrum and then substituted into Eq. (14) to calculate β. The vibration amplitude calculated from the spectrum in Fig. 2(c) is indicated by the red dot in Fig. 2(d). This procedure is repeated for each depth in the sample, allowing a vibration amplitude plot (blue line in Fig. 2(d)) to be generated. As expected for this mechanically homogeneous sample, the vibration amplitude decreases approximately linearly with depth. 2D vibration amplitude images and elastograms can be obtained by repeating this procedure whilst scanning the beam over the surface of the sample, which is demonstrated in Section 4.

3.3.2. Phase-sensitive OCE

In Fig. 3, the same data used to generate the results shown in Fig. 2 are used to describe the processing procedure for phase-sensitive OCE. Figure 2(a) is reproduced in Fig. 3(a), for convenience. Figure 3(b) shows the image generated by calculating the phase difference between consecutive A-scans, after performing a Fourier transform in wavenumber. The bright/dark banding in time is caused by loading-induced motion. Figure 3(c) shows the spectrum of the phase difference obtained by performing a Fourier transform in time, at the depth indicated by the red line in Fig. 3(b). The red lines in Fig. 3(b) and Fig. 2(b) indicate the same depth. In this spectrum, the peak corresponding to the vibration frequency is clearly visible at 50 Hz. A second peak, due to galvanometer jitter, is also visible at approximately 160 Hz. The vibration amplitude is calculated from the spectrum using Eq. (19). The vibration amplitude corresponding to the spectrum in Fig. 3(c) is indicated by the red dot in Fig. 3(d).

This procedure is repeated for each depth in the sample, allowing a vibration amplitude plot (blue line in Fig. 3(d)) to be generated. Similarly to Fig. 2(d), in Fig. 3(d) the vibration amplitude decreases approximately linearly with depth from an initial value of ~0.35 μm. Comparing the two figures, it can be seen that the accuracy of the vibration amplitude measured using the phase difference method is much lower than the STd method at depths >0.8 mm, as indicated by large negative fluctuations in vibration amplitude in Fig. 3(d). This

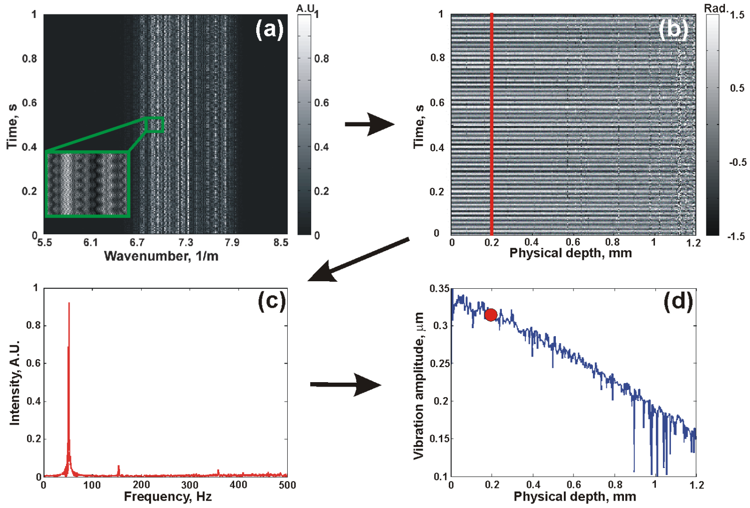

Fig. 3. Data processing procedure for phase-sensitive OCE: (a) 2000 spectral interferograms resampled to *k*-space; (b) Phase difference image obtained after Fourier transform in *k*-space; (c) Phase difference spectrum after Fourier transform in time, at depth indicated by the red line in (b); and (d) Vibration amplitude calculated using the analysis presented in [21]. The red dot corresponds to the vibration amplitude calculated from the phase difference spectrum in (c).

is related to the probability density functions (PDFs) for phase and amplitude and is discussed in detail in Section 4.1.

3.3.3. Elastogram generation

Elastograms were generated from 128 vibration amplitude plots, recorded whilst scanning the beam over a lateral range of 3 mm. Each vibration amplitude plot was generated using 1000 A-scans. To generate elastograms, the strain was calculated over an axial range of 75 μm. Each pixel in an elastogram corresponds to the strain calculated at that location normalized to the maximum strain in the elastogram.

4. Results

4.1. Vibrating mirror

Figure 4 shows the measured vibration amplitude of an oscillating mirror, determined using the STd and phase-sensitive methods on the same 2000 A-scans, versus the OCT SNR, which was varied using neutral density filters. Figure 4 shows the mean vibration amplitude (±1 standard deviation) calculated from ten consecutive measurements. For the STd method, we observe a relatively constant vibration amplitude; whereas, the phase-sensitive method significantly underestimates the vibration amplitude for low OCT SNR. At the highest OCT SNR of 55 dB, the mean vibration amplitude of the mirror measured using both methods was 0.43 μm. The standard deviation of the phase-sensitive and STd methods was 1.5 nm and 2.7 nm, respectively. As the standard deviation may be considered to represent the vibration amplitude sensitivity [12], this result indicates that for high SNR, phase-sensitive OCE provides more precise measurements. This result is explained by considering the respective PDFs of phase and amplitude [29]. For high OCT SNR, the phase PDF tends towards a delta function, whilst the amplitude PDF is approximated by a Gaussian distribution, with variance determined by the shot noise of the system. However, the situation changes dramatically as the OCT SNR decreases. The phase PDF tends towards a uniform distribution, resulting in much lower phase sensitivity. This leads to a significant increase in the incidence of phase wrapping, causing the measured vibration amplitude in the phase-sensitive method to tend towards zero, thus, underestimating the true value. However, the amplitude PDF continues to be approximated by an unbiased Gaussian distribution with constant variance whenever the OCT SNR > ~5 dB – a clear advantage of STdOCE. For example, in Fig. 4, at OCT SNR = 5 dB the mean vibration amplitude measured using the phase-sensitive and STd methods are ~0.34 μm and ~0.42 μm, respectively. This underestimation of the mean vibration amplitude using the phase-sensitive method is consistent with previously presented results in flow imaging [29]. Using the vibration amplitude measured with the phase-sensitive method at OCT SNR = 55 dB as the best estimate of the mirror's true vibration amplitude, at OCT SNR = 5 dB, the phase-sensitive method underestimates the vibration amplitude by >20%, whereas, STdOCE underestimates it by <3%.

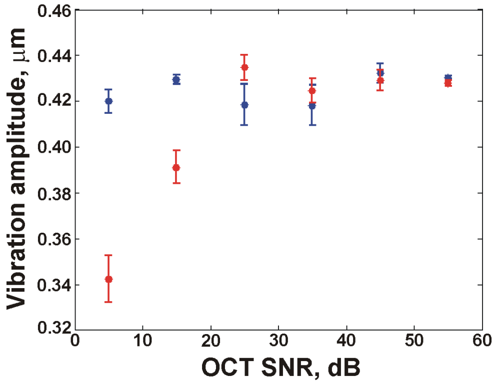

Fig. 4. Vibration amplitude (±1 SD) of a mirror measured using STdOCE (blue) and phase-sensitive OCE (red) versus OCT SNR.

It should be noted that for OCT SNR < 5 dB, STdOCE will also introduce significant errors in the vibration amplitude measurement as, in this case, the amplitude PDF will approach a Rayleigh distribution. The pertinent point is that this error occurs for much lower SNR than in the phase-sensitive method.

For OCE imaging of turbid samples, in which the OCT SNR decreases with depth due to attenuation, the results in Fig. 4 indicate that STdOCE should provide accurate measurement of vibration amplitude over a larger depth range than the phase-sensitive method, which we shall confirm in the next section. This result also indicates that in elastograms generated using the phase-sensitive method, the strain calculated in regions of low OCT SNR (<20 dB) will be artificially high, due to underestimation of the vibration amplitude. This is discussed in more detail in the next section.

4.2. Elastograms

In this section, we present 2D elastograms generated using both STd and phase-sensitive methods applied to the same data. In each case, the vibration amplitude of the unloaded ring actuator was measured using both methods to be 0.35 μm.

4.2.1. Phantom 2: Soft with hard inclusions

A structural OCT image of Phantom 2 is shown in Fig. 5(a). The inclusion is located in the center of the image and is indicated by the labeled arrow in the figure. Below the inclusion, a shadow artifact, corresponding to a region of low OCT SNR, is also labeled. A plot of the OCT SNR at the lateral position indicated by the vertical red arrow in Fig. 5(a) is shown in Fig. 5(d). In this plot, the large slope of the OCT SNR with depth in the inclusion indicates high attenuation, as expected due to the increased concentration of scatterers in this feature.

Vibration amplitude images generated using the STd and phase-sensitive methods are shown in Figs. 5(b) and 5(f), respectively. In both images, the stiff inclusions are visible due to a lower rate of change in vibration amplitude with depth, *i.e.*, lower strain, in this feature.

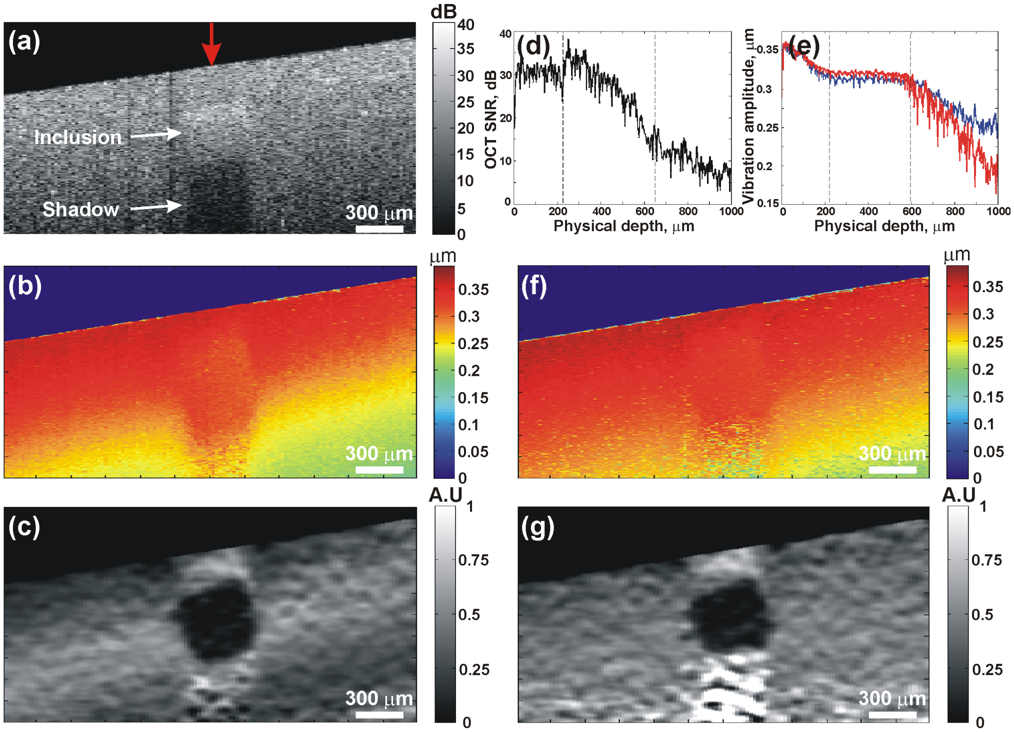

Fig. 5. Phantom 2: (a) OCT structural image; (b) Vibration amplitude image; and (c) Elastogram for STdOCE; (d) OCT A-scan; and (e) Vibration amplitude plots for STdOCE (blue) and phase-sensitive OCE (red) at the lateral position indicated by the red arrow in (a), where the dashed lines in (d) and (e) indicate the boundaries between the soft bulk and hard inclusion; (f) Vibration amplitude image; and (g) Elastogram for phase-sensitive OCE.

Vibration amplitude plots generated using both methods, at the lateral position indicated by the red arrow in Fig. 5(a), are shown in Fig. 5(e). Both plots match well until a depth of ~600 µm. At depths >600 µm, the decrease in vibration amplitude is higher for the phase-sensitive method (red). This is caused by an underestimation of the vibration amplitude in the low OCT SNR region below the inclusion (see Subsection 4.1) and results in an artificially high value of calculated strain. This result is discussed in greater detail in Section 5.

The elastograms corresponding to Figs. 5(b) and 5(f) are shown in Figs. 5(c) and 5(g), respectively. The artificially high strain in the phase-sensitive elastogram (Fig. 5(g)) is clearly visible below the inclusion. As the elastogram is used as a surrogate for elasticity, this leads to errors in the interpretation of elastograms. For example, in Fig. 5(g), the region below the inclusion is incorrectly presented as having a significantly lower stiffness than the surrounding soft material.

4.2.2. Porcine tissue

To demonstrate STdOCE on tissue, we performed measurements on freshly excised porcine tissue. A flat 10 mm × 10 mm × 2.5 mm section of tissue taken from the chest wall was positioned in our OCE system. A representative histology slice taken after OCT/OCE imaging is shown in Fig. 6(a). Two tissue types can clearly be identified in this image. A thin soft layer approximately 150 µm thick is visible near the surface of the tissue. This layer corresponds to adventitia. The underlying stiffer thick layer is intercostal muscle. The corresponding OCT structural image is shown in Fig. 6(d). The two layers distinguishable in the histology slice can readily be seen in this image: with the thin adventitia layer having a higher OCT SNR than the underlying muscle. The vibration amplitude images obtained using STdOCE (Fig.

6(b)) and phase-sensitive OCE (Fig. 6(e)) are also shown. The corresponding elastograms are shown in Figs. 6(c) and 6(f). The two layers visible in the histology and OCT images can be distinguished in both elastograms. Higher strain is present in the softer thin layer in comparison to the stiffer underlying tissue, as expected. However, the strain contrast between the layers is significantly higher for STdOCE than for phase-sensitive OCE. The strain measured in the thin layer is similar using both techniques. However, much higher strain is visible in the thicker layer using the phase-sensitive method. This higher strain is caused by underestimation of the vibration amplitude measurements using this method due to low OCT SNR in the thick layer. The elastograms presented in Fig. 6 demonstrate the improvement in quality obtained using STdOCE in comparison to phase-sensitive OCE.

This advantage can also be seen in Fig. 7, which shows the OCT SNR (Fig. 7(a)) and vibration amplitude (Fig. 7(b)) plots corresponding to the lateral position indicated by the arrow in Fig. 6(d). Figure 7(a) confirms the high OCT SNR in the thin layer, as well as the significant decrease in OCT SNR in the thick layer. Figure 7(b) shows the corresponding vibration amplitude plots obtained using STdOCE (blue) and phase-sensitive OCE (red). The vibration amplitude measured using both methods matches well until a depth of ~480 μm. At depths >480 μm, a significantly larger slope (strain) is observed in the phase-sensitive plot. This change in slope does not correspond to any structural changes visible in either the histology or the OCT images and is caused by the low OCT SNR at these depths. It is this artificial increase in strain that reduces the contrast between the two layers in the corresponding phase-sensitive elastogram (Fig. 6(f)). In contrast, it can be seen in Fig. 7(b) that the STdOCE vibration amplitude plot (blue) maintains a relatively constant slope at depths up to 720 μm, indicating that the thick layer is mechanically uniform. For the result presented in Fig. 7, we observe a ~50% increase in the depth range over which reliable vibration amplitude measurements are obtained using STdOCE in comparison to phase-sensitive OCE.

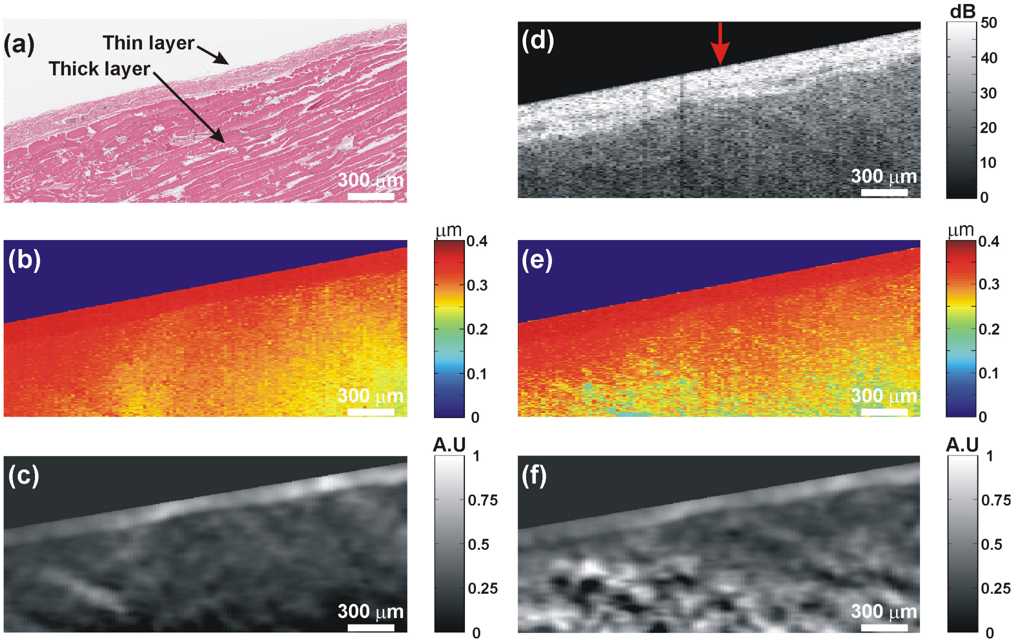

Fig. 6. Porcine tissue: (a) Histology; (b) Vibration amplitude image; and (c) Elastogram for STdOCE; (d) OCT structural image. The red arrow indicates the location of the plots in Fig. 7; (e) Vibration amplitude image; and (f) Elastogram for phase-sensitive OCE.

#175397 - $15.00 USD Received 31 Aug 2012; revised 5 Nov 2012; accepted 5 Nov 2012; published 7 Nov 2012

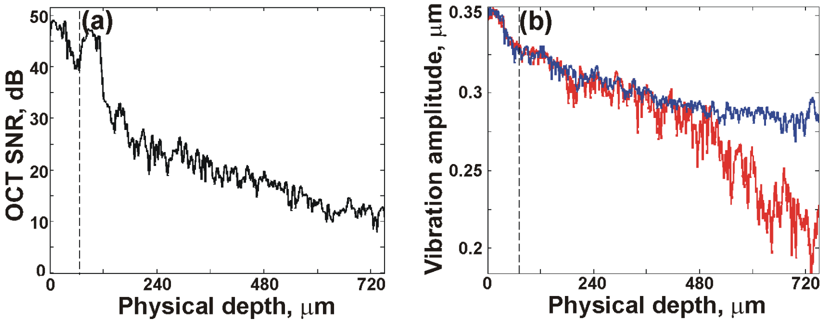

Fig. 7. (a) OCT A-scan; and (b) Vibration amplitude plots of porcine tissue for STdOCE (blue) and phase-sensitive OCE (red), at lateral position indicated by the red arrow in Fig. 6(d). The dashed lines in (a) and (b) indicate the boundary between tissue layers.

5. Discussion

In this paper, we have presented a new method to extend the performance of dynamic OCE in regions of the elastogram corresponding to low OCT SNR. From the experimental data presented in Fig. 4, the accuracy of STdOCE exceeds that of phase-sensitive OCE for OCT SNRs below ~20 dB. Since the OCT SNR is often below 20 dB, this improvement will lead to a marked general improvement in elastograms.

In Subsection 4.2.1, we experimentally confirmed the systematic underestimation of vibration amplitude in regions in a phantom corresponding to low OCT SNR (see Fig. 5). The soft material in the inclusion phantom has uniform elasticity [5], thus, assuming uniform stress in this material, the strain above and below the inclusion should ideally be the same. From Fig. 5(e) (blue curve), the strain measured with STdOCE approximates this ideal case well, with strains of 4.1×10^{-4} and 3.9×10^{-4} measured above and below the inclusion, respectively, versus 3.8×10^{-4} and 6.1×10^{-4} with the phase-sensitive method (red curve). Secondly, as the phantom has uniform elasticity at depths beneath the inclusion, *i.e.*, >600 µm, the true vibration amplitude will decay linearly with depth from this point, reducing to zero at the opposite surface of the phantom, *i.e.*, at a depth of 2.5 mm, corresponding to the thickness of the loaded sample. If we extrapolate the linear decay in vibration amplitude visible in Fig. 5(e) for depths >600 µm, we predict, based on STdOCE, zero vibration amplitude at a depth of ~2.5 mm, as expected. Performing the same analysis for phase-sensitive OCE, we incorrectly predict zero vibration amplitude at a depth of ~2.1 mm, 0.4 mm from the sample boundary.

As comparisons made between phase-sensitive and STd methods are based on the same data, the data acquisition time was the same for both methods. STdOCE relies on the analysis of multiple frequency tones, thus, dense sampling is required to adequately sample each tone. In comparison, phase-sensitive OCE analyzes the phase difference spectrum, consisting of a single frequency component. The vibration amplitude can be estimated using the phase-sensitive method once the A-scan acquisition frequency exceeds twice the excitation frequency [17], at the expense of lower accuracy for less densely sampled data [21]. As the acquisition speed of OCT systems increases and more sophisticated signal processing hardware, *e.g.*, graphics processing units (GPUs) become available, the dense sampling required for STdOCE will become more practical and efficient.

Many related OCT techniques and applications rely on vibration amplitude measurement: for imaging vibrations of the vocal chords [41,42] and the ear [21,43,44]; in functional imaging techniques such as magneto-motive OCT [19]; and for photothermal OCT [20]. The method presented in this paper could readily be applied in such techniques to improve the accuracy of vibration amplitude measurement.

6. Conclusions

We have presented a new method to measure vibration amplitude in dynamic optical coherence elastography based on analysis of the Doppler spectrum. We have demonstrated that our method is more robust for low OCT SNR than the currently used phase-sensitive method. Vibration amplitude measurements performed on a vibrating mirror when the OCT SNR was held constant at 5 dB demonstrate <3% error in comparison to >20% using the currently employed phase-sensitive method. Elastograms of a tissue-mimicking phantom and excised porcine tissue demonstrate improvements in quality with this new method, including a 50% increase in the depth range of reliable vibration amplitude. Such improvements increase the clinical potential of this emerging modality.

Acknowledgments

The authors thank Dr. Robert McLaughlin and Dr. Peter Noble for organizing the tissue imaging. B. F. K. acknowledges support from the Raine Medical Research Foundation; M. W. from a UWA Gledden Visiting Senior Fellowship, the European Heads of Research Councils (EuroHORCs) and the European Science Foundation (ESF—EURYI 01/2007PL) operated by the Foundation for Polish Science; M. S. from the Polish Ministry of Science and Higher Education (2010-2014); and K. M. K. from the Scholarship for International Research Fees and University International Stipend, UWA.

#175397 - $15.00 USD Received 31 Aug 2012; revised 5 Nov 2012; accepted 5 Nov 2012; published 7 Nov 2012